SPANDIDOS PUBLICATIONS
ONCOLOGY REPORTS 41: 2636-2646, 2019

The PI3K inhibitor buparlisib suppresses osteoclast formation and tumour cell growth in bone metastasis of lung cancer, as evidenced by multimodality molecular imaging

SHENGFEI WANG[1,2*], XIAOMIN NIU[3*], XIAO BAO[2,4-7], QIN WANG[8], JIANPING ZHANG[2,4-6],
SHUN LU[3], YONGJUN WANG[9], LING XU[8], MINGWEI WANG[2,4-6] and JIE ZHANG[1,2,10]

[1]Department of Thoracic Surgery, Fudan University Shanghai Cancer Center, Shanghai 200032;
[2]Department of Oncology, Shanghai Medical College, Fudan University, Shanghai 200433;
[3]Department of Shanghai Lung Cancer Center, Shanghai Chest Hospital, Shanghai Jiao Tong University,
Shanghai 200030; [4]Department of Nuclear Medicine, Fudan University Shanghai Cancer Center, Shanghai 200032;
[5]Center for Biomedical Imaging, Fudan University, Shanghai 200433; [6]Shanghai Engineering Research Center of
Molecular Imaging Probes, Shanghai 200032; [7]Department of Radiology, Shanghai Pulmonary Hospital, Tongji University,
Shanghai 200433; [8]Department of Oncology, Yueyang Hospital Affiliated to Shanghai University of
Traditional Chinese Medicine, Shanghai 200437; [9]Department of Orthopaedics and Traumatology,
Longhua Hospital Affiliated to Shanghai University of Traditional Chinese Medicine, Shanghai 200000, P.R. China;
[10]Department of Cardiothoracic Surgery, University of Pittsburgh Medical Center, Pittsburgh, PA 15232, USA

Received August 3, 2018; Accepted March 4, 2019

DOI: 10.3892/or.2019.7080

Abstract. Non-small cell lung cancer (NSCLC) metastasis commonly occurs in bone, which often results in pathological fractures. Sustained phosphoinositide-3-kinase (PI3K) signalling promotes the growth of PI3K-dependent NSCLC and elevates osteoclastogenic potential. The present study investigated the effects of a PI3K inhibitor on NSCLC growth in bone and osteoclast formation, and aimed to determine whether it could control symptoms associated with bone metastasis. A bone metastasis xenograft model was established by implanting NCI-H460-luc2 lung cancer cells, which contain a phosphatidylinositol-4,5-bisphosphate 3-kinase catalytic subunit α mutation, into the right tibiae of mice. After 1 week, the tumours were challenged with a PI3K inhibitor (buparlisib) or blank control for 3 weeks. Tumour growth and burden were longitudinally assessed *in vivo* via reporter gene bioluminescence imaging (BLI), small animal positron emission tomography/computed tomography (CT) [^{18}F-fluorodeoxyglucose (^{18}F-FDG)] and single-photon emission computed tomography/CT [^{99m}Tc-methylene diphosphonate (^{99m}Tc-MDP)] imaging. Tibia sections of intraosseous NCI-H460 tumours were analysed by immunohistochemistry (IHC), western blotting and flow cytometry. Dynamic weight bearing (DWB) tests were further performed to examine the improvement of symptoms associated with bone metastasis during the entire study. Administration of buparlisib significantly inhibited the progression of bone metastasis of NSCLC, as evidenced by significantly reduced uptake of ^{18}F-FDG, ^{99m}Tc-MDP and BLI signals in the treated lesions. In addition, buparlisib appeared to inhibit the expression of tartrate-resistant acid phosphatase and receptor activator of nuclear factor-κB ligand, as determined by IHC. Buparlisib also resulted in increased cell apoptosis, as determined by a higher percentage of Annexin V staining and increased caspase 3 expression. Furthermore, buparlisib significantly increased weight-bearing capacity, as revealed by DWB tests. The PI3K inhibitor, buparlisib, suppressed osteoclast formation *in vivo*, and exhibited antitumour activity, thus leading to increased weight-bearing ability in mice with bone metastasis of lung cancer. Therefore, targeting the PI3K pathway may be a potential therapeutic strategy that prevents the structural skeletal damage associated with bone metastasis of lung cancer.

Correspondence to: Dr Jie Zhang, Department of Thoracic Surgery, Fudan University Shanghai Cancer Center, 270 Dong'an Road, Shanghai 200032, P.R. China
E-mail: zhangjie2289@hotmail.com

Dr Mingwei Wang, Department of Nuclear Medicine, Fudan University Shanghai Cancer Center, 270 Dong'an Road, Shanghai 200032, P.R. China
E-mail: wang.mingwei88@163.com

[*]Contributed equally

Key words: non-small cell lung cancer, bone metastasis, phosphoinositide-3-kinase inhibitor, multimodality molecular imaging, multiparametric quantification

Introduction

Lung cancer remains one of the most common causes of cancer-associated mortality worldwide (1). Non-small cell lung cancer (NSCLC) represents ~85% of total lung cancer cases, and has an overall 5-year survival rate of 17.1% (2,3). NSCLC frequently metastasizes to the bone, brain, other lung regions and the liver; bone metastases account for ~39% of total incidence (4). At present, bone is the third most common site of metastatic disease after the lung and liver, and the most common types of primary cancer are lung, breast, prostate, thyroid and renal cancer (5). Pathological fractures caused by skeletal metastases in patients with lung cancer are additional obstacles, since impending or actual pathological fractures in patients with metastatic bone tumours are a difficult and challenging complication that affect management and prognosis, decrease quality of life and jeopardize survival (6,7).

Stabilization of an impending or actual pathological fracture involves techniques and concepts that differ from those used to treat patients with non-pathological fractures (8). Bisphosphonates are a class of drugs that prevent the loss of bone mass, which are used to treat and reduce the risk of fracture and bone pain (9) in patients with lung cancer (10) and other metastatic cancers, including breast cancer, prostate cancer and multiple myeloma (MM) (11,12). Previous studies have demonstrated that differential expression of receptor activator of nuclear factor (NF)-κB (RANK), RANK ligand (RANKL) and the protein osteoprotegrin (OPG) are associated with the metastatic potential of human NSCLC to the bone, raising the possibility that the RANK/RANKL/OPG pathway may be a therapeutic target for the treatment of NSCLC patients with bone metastases (13,14). Research has recently focused on the treatment of bone metastasis of lung cancer, in order to explore novel treatment strategies to reduce the incidence of pathological fractures.

The phosphoinositide-3-kinase (PI3K)/mammalian target of rapamycin (mTOR)/protein kinase B (AKT) pathway is frequently dysregulated in cancer (15-17), and mTOR is activated in >50% of lung cancer cases (18). Preclinical studies have suggested that inhibition of the PI3K pathway and its components may inhibit the growth of PI3K-dependent NSCLC cell lines, and reduce tumour growth in mouse xenograft models of PI3K-driven lung cancer (19-22). However, it remains to be elucidated as to whether PI3K inhibitors target bone metastasis of lung cancer, and reduce osteoclast generation and bone destruction. The present study aimed to investigate the *in vivo* potential of a PI3K inhibitor to inhibit growth and metastasis of highly metastatic NCI-H460-luc2 lung cancer cells, which were implanted into the right tibiae of mice. The effects of the PI3K inhibitor were monitored by *in vivo* multimodality molecular imaging via small animal positron emission tomography (PET)/computed tomography (CT) [^{18}F-fluorodeoxyglucose (^{18}F-FDG)], single-photon emission computed tomography (SPECT)/CT [^{99m}Tc-methylene diphosphonate (^{99m}Tc-MDP)] and reporter gene bioluminescence imaging (BLI). Furthermore, dynamic weight bearing (DWB) tests were used to examine the improvement of symptoms associated with bone metastasis.

Materials and methods

PI3K inhibitor (buparlisib) and human lung cancer cell line (NCI-H460-luc2). Buparlisib (NVP-BKM120; Novartis International AG, Basel, Switzerland) is an oral pyrimidine-derived PI3K inhibitor that targets all isoforms of Class I PI3K (α, β, γ and δ) with high selectivity (23). Buparlisib was dissolved in N-methyl-2-pyrrolidone (NMP), then diluted with nine volumes of polyethylene glycol (PEG) 300 to obtain a 1:9 NMP/PEG300 solution. The buparlisib-sensitive cell line NCI-H460-luc2 (Bioware® Ultra-Light Producing Cell Line; Cold Spring Biotech Corp., Shanghai, China) was used in this study. This cell line is a highly metastatic lung cancer cell line stably transfected with the firefly luciferase gene (luc2), which was established by transducing a lentivirus containing the luc2 gene under the control of the human ubiquitin C promoter; this cell line carries a phosphatidylinositol-4,5-bisphosphate 3-kinase catalytic subunit (PIK3CA; c.1633G>A; p.E545K) missense mutation (24).

Animal model establishment. A total of 20 nude mice (50% male and 50% female; BALB/c nu/nu; age, 6 weeks; weight, 18-25 g; Shanghai Laboratory Animal Center of the Chinese Academy of Science, Shanghai, China) were divided into two groups: The NMP/PEG300 control group (n=10) and the buparlisib treatment group (n=10). Animals were acclimated to the animal facility for 1 week prior to surgery under a 12-h light/dark cycle, with *ad libitum* access to food and water in a specific pathogen-free environment (10-25˚C; 20-25 Pa; 40-70% humidity). For each mouse, 1.0×10^8/ml NCI-H460 cells were inoculated into the right tibia using an optimized procedure based on a general method (25). Briefly, under appropriate anaesthetic depth, the mice were fixed in a position where the right tibia was fully exposed, and flexion with tibia to femur was in the 90-degree position. Along the direction of the lateral border of the tibia, the needle was injected through the tibial cancellous bone into the marrow cavity from the centre of the tibial plateau using an empty BD insulin syringe (U40; 1 ml; 29 g x 12.7 mm; diameter, 0.30 mm; BD Biosciences, Franklin Lakes, NJ, USA). The needle was gently pulled out to release the pressure of the marrow cavity. A gaseous microsyringe (25 µl; diameter, 0.50 mm) was used to inject the NCI-H460 cell suspension (10 µl; 1×10^8 cells/ml), air (1 µl) and gel foam (2 µl) along the original injection site. The injection site was then compressed for seconds for haemostasis. The present study was approved by the ethics committee of Fudan University Institutional Animal Care (Shanghai, China) and Longhua Hospital, Shanghai University of Traditional Chinese Medicine (Shanghai, China). The use of animals and the experimental protocol were approved by the Institutional Animal Care and Use Committee of Longhua Hospital, Shanghai University of Traditional Chinese Medicine. All experiments were performed in accordance with relevant guidelines and regulations for the welfare and use of animals in cancer research.

Treatment protocol. A total of 1 week after tumour cell inoculation in mice, and confirmation of tumour growth in the bone by optical imaging, within 30-60 min of buparlisib NMP/PEG300 preparation, the mice were treated with buparlisib NMP/PEG300 or control NMP/PEG300 solutions. At 0, 1 and 3 weeks, mice were treated via gavage, as follows: i) Buparlisib group: 200 µl buparlisib NMP/PEG300 solution (30 mg/kg/day); ii) Control group: 200 µl control NMP/PEG300 solution; mice in the control group were treated with the same volume as the treatment group. All treatments adhered to a

5-days-on and 2-days-off cycle, with body weight and tumour growth in the right tibia monitored weekly. At the end of the study, mice were sacrificed and the right tibiae were removed.

MicroPET/CT imaging. MicroPET/CT scans were performed using Inveon MicroPET/CT (Siemens AG, Munich, Germany) on weeks 0, 1 and 3 after therapy initiation (Fig. 1A). All mice were fasted overnight prior to probe injection, and were maintained under isoflurane anaesthesia and kept warm during the injection, accumulation and scanning periods. Each mouse was injected with 11.1 MBq (300 μCi) ^{18}F-FDG via the tail vein. Subsequently, 10-min static images were acquired 1 h post-injection. PET/CT images were visualized and analysed using Inveon Research Workplace software (Siemens AG). To determine the level of variation in radiotracer uptake, the maximal standardized uptake value (SUVmax) was calculated according to the following formulas: SUV was calculated within the boundaries of a region of interest (ROI), which was delineated on the CT images of the cancer cell-implanted tibia. In addition, the ratio of right tibia to left tibia SUVmax (R/L ratio) was calculated, since no NCI-H460 tumour cells were inoculated into the left tibiae; this value was used as a standard reference value. Tibiae were removed once the mice had been sacrificed. Subsequently, *ex vivo* MicroCT analysis was conducted from the tibial plateau to the tibial internal condyle, and 3D structures were reconstructed using the Inveon analysis workstation (V2; Siemens AG). The cancellous bone region of the femoral head was used as a region of interest for quantitative calculations. Bone volume/total volume, trabecular thickness, trabecular number and trabecular separation were calculated using the Inveon analysis workstation.

MicroSPECT/CT imaging. To better observe the bone, ^{99m}Tc-MDP SPECT/CT scanning was performed on weeks 0, 1 and 3 following treatment (Fig. 1A) using a small animal SPECT/CT device (Bioscan, Inc, Poway, CA, USA). Briefly, 111 MBq (3 mCi) ^{99m}Tc-MDP was intravenously injected into the caudal region. ^{99m}Tc-MDP first binds to the unmineralized extracellular matrix of newly formed bone and is subsequently irreversibly incorporated into the mineralized extracellular matrix. A total of 4 h post-injection, MicroSPECT/CT images were acquired using tomographic data acquisition in 10-20 sec/projections for 30 projections. CT was acquired in 512 projections to allow anatomic coregistration. Data reconstruction and analysis were performed using the ordered-subsets expectation maximization algorithm and InVivoScope1.42 software (Bioscan, Inc).

BLI. Bioluminescent images were acquired using an IVIS Lumina II Spectrum (PerkinElmer, Inc., Waltham, MA, USA) on weeks 0, 1 and 3 after therapy initiation (Fig. 1A). In preparation for *in vivo* imaging, anaesthesia was induced in mice by exposing them to 2-3% isoflurane in an oxygen-filled induction chamber. Once anesthetized, the mice were transferred to an isolation chamber, then placed in the imaging chamber and connected to the in-chamber anaesthesia delivery system, which was maintained at 1-2% isoflurane. Bioluminescent signals were represented in the images with a pseudo-colour scale ranging from red (most intense) to violet (least intense) indicating the intensity of the signal. Scales were manually adjusted to the same values for each comparable image (*in vivo*) to normalize the intensity of bioluminescence across time points.

Immunohistochemical staining and histological procedures. Immunohistochemical staining and histological procedures were carried out 3 weeks after therapy initiation (Fig. 1A). Animals were deeply anesthetized with 5% isoflurane and were sacrificed, after which right tibia specimens were removed and maintained at 4˚C in 4% paraformaldehyde in phosphate buffer (0.1 M, pH 7.4) for 3 days. Subsequently, the specimens were transferred to EDTA decalcifying solution (0.5 M, pH 8.0, cat. no. G1105; Wuhan Servicebio Co., Ltd., Wuhan, China) for 1 month, processed and embedded in paraffin. Longitudinal midsagittal sections (size, 4 μm) of all tissues were prepared for staining. Images of haematoxylin and eosin (H&E) staining were captured using a Leica DMI3000B microscope (Leica Microsystems GmbH, Wetzlar, Germany), whereas images of tartrate-resistant acid phosphatase (TRAP) and RANKL staining were captured using a Nikon ECLIPSE TI-SR microscope (Nikon Corporation, Tokyo, Japan).

For H&E staining (cat. no. G1005; Wuhan Servicebio Co., Ltd.), paraffin-embedded slides were dewaxed in xylene, rehydrated with decreasing concentrations of ethanol, washed in PBS and stained with Harris's hematoxylin (10%) for 3-8 min and eosin (70%) for 1-3 min at room temperature. Subsequently, sections were dehydrated through an increasing concentration of ethanol and xylene.

TRAP staining was carried out using the kit (cat. no. GP1046; Wuhan Servicebio Co., Ltd.) according to the manufacturer's protocol. Briefly, prior to staining, paraffin-embedded slides were dewaxed and hydrated, followed by incubation with a mix prepared according to the manufacturer's protocol for 1 h at 37˚C. Finally, tibia slides were stained with hematoxylin for 3 min and washed twice in slowly running tap water. In cells positively stained for TRAP, the cytoplasm of osteoclasts was stained a red-violet colour.

For RANKL staining, paraffin-embedded right tibia slides were deparaffinized and rehydrated. The samples were immersed in citrate antigen retrieval solution (pH 6.0) and maintained at sub-boiling temperature (95-100˚C) for 15 min to unmask antigenicity. Subsequently, slides were rinsed with PBS containing 3% H_2O_2 and incubated at room temperature for 15 min in the dark to inhibit endogenous peroxidase activity. Subsequently, the slides were blocked with 3% bovine serum albumin (cat. no. G5001; Wuhan Servicebio Co., Ltd.) at room temperature for 30 min and were incubated with a rabbit anti-RANKL primary antibody (1:100 dilution, cat. no. GB11235; Wuhan Servicebio Co., Ltd.) overnight at 4˚C. The samples were subsequently washed with PBS, incubated at room temperature for 50 min with horseradish peroxidase (HRP)-conjugated secondary antibodies (1:200 dilution, cat. no. GB23303; Wuhan Servicebio Co., Ltd.), and treated with DAB chromogenic reagent to visualize tissues. Once the nuclei exhibited brown-yellow staining, samples were counterstained with hematoxylin staining solution for 3 min and washed in tap water. Finally, samples were dehydrated in ascending alcohol concentrations and cleared with xylene. All regions shown on the histological slices were in the metaphysis, anterior to the growth plate in bone regions where resorption was important.

Apoptosis assay. An apoptosis assay was carried out 3 weeks after therapy initiation (Fig. 1A). Apoptosis was measured by flow cytometry using the Annexin V fluorescein isothiocyanate (FITC) Apoptosis Detection kit I (cat. no. 556547; BD Pharmingen; BD Biosciences). Each group was analysed five times. Briefly, each excised xenograft was cut into multiple 1x1x1 mm^3 pieces within 30 min of surgical removal at 4°C, washed with aseptic salt water and filtered through a 200-μm mesh sieve to prepare a single cell suspension. Annexin V FITC staining was conducted as follows: Cells were washed twice with cold PBS and resuspended in 1X binding buffer at a concentration of $1x10^6$ cells/ml. Cells (100 μl, $1x10^5$) were then transferred to a 5 ml culture tube, 5 μl FITC Annexin V and 5 μl propidium iodide were added, and cells were gently vortexed and incubated for 15 min at room temperature (25°C) in the dark. Finally, 400 μl 1X binding buffer was added to each tube and analysed immediately by flow cytometry (BD FACSuite™; BD Biosciences) within 1 h.

For terminal deoxynucleotidyl transferase (TdT)-mediated deoxyuridine triphosphate nick end labelling (TUNEL) staining, tibia samples were cut into longitudinal sections and were analysed using the In-Situ Cell Death Detection kit (cat. no. Roche-11684817910; Sigma-Aldrich; Merck KGaA, Darmstadt, Germany), according to the manufacturer's protocol. Briefly, prior to staining, paraffin-embedded slides were dewaxed and hydrated, underwent antigen retrieval in proteinase K solution (1:10 dilution, cat. no. G1205; Wuhan Servicebio Co., Ltd.) at 37°C for 15 min, and were permeabilized for 25 min at room temperature using Triton X-100 (cat. no. G1204; Wuhan Servicebio Co., Ltd.). The tibia slides were then incubated with TdT and fluorescein-labelled deoxyuridine triphosphate for 3-4 h at 37°C, followed by incubation with DAPI in the dark for 10 min at room temperature to identify the nuclei. TUNEL and DAPI staining was observed under a fluorescence microscope (Olympus Corporation, Tokyo, Japan). To quantitatively analyse the number of apoptotic cells, TUNEL-positive cells were counted by three independent researchers. Means of the intensity of green fluorescence was calculated using Image-Pro Plus (version 6.0.0.260; Media Cybernetics, Inc., Rockville, MD, USA). The proportion of TUNEL-positive cells compared with the number of total cells was calculated as the percentage of apoptotic cells.

Western blotting. Protein samples were extracted from xenografts arising in the metaphysis of the upper tibia, which broke through the bone cortex and extended into soft tissue. Total protein was extracted using radioimmunoprecipitation assay lysis buffer (cat. no. G2002; Wuhan Servicebio Co., Ltd.) and protein concentration was determined via bicinchoninic acid protein assay using a quantification kit (cat. no. G2026; Wuhan Servicebio Co., Ltd). Proteins (40 μg) were separated by 10% SDS-PAGE and were electrophoretically transferred to polyvinylidene fluoride membranes (EMD Millipore, Billerica, MA, USA). After blocking with 5% fat-free milk at room temperature for 2 h, the membranes were probed with the following primary antibodies (1:1,000 dilutions): Caspase 3 (cat. no. BS1518; Bioworld Technology, Inc., St. Louis Park, MN, USA), B-cell lymphoma 2 (Bcl-2; cat. no. 2870; Cell Signaling Technology, Inc., Danvers, MA, USA) and Bcl-2-associated X protein (Bax; cat. no. GB11690; Wuhan Servicebio Co., Ltd.) overnight at 4°C. Subsequently, membranes were incubated with a HRP-conjugated immunoglobulin G secondary antibody (1:3,000 dilution, cat. no. GB23303; Wuhan Servicebio Co., Ltd.) at room temperature for 2 h. Blots were developed using an enhanced chemiluminescence kit (cat. no. G2019; Wuhan Servicebio Co., Ltd.) and band intensity was semi-quantified with AlphaEaseFC (ProteinSimple, San Jose, CA, USA). β-actin (cat. no. GB11001, Wuhan Servicebio Co., Ltd.) served as a loading control.

DWB test. The DWB apparatus consisted of a small Plexiglas chamber (11x11 cm) with a floor sensor containing 1,936 pressure transducers. A camera was pointed at the side of the enclosure to assist with data analysis. The system used software (Dynamic Weight Bearing 1.4.1.23; Bioseb, Pinellas Park, FL, USA), which recorded, in grams, the average weight that each limb exerted on the floor, without any interference of the analyser. To test the weight-bearing capacity, the mouse was placed in the chamber and allowed to move freely within the apparatus for a 2-min test period. The amount of weight that passed through each paw was assessed automatically using the pressure transducers. All movements were manually validated by the experimental operators, in accordance with the position of the mouse on the device using the synchronized video as a reference, to ensure that the correct paw corresponded to the set of pixels recognized by the sensors. The DWB software provided data regarding the weight (in grams) and the averaged values of right/left (R/L) raw pressure (26).

Statistical analysis. Data are presented as the means ± standard deviation. The effects of treatment at each time-point were evaluated using a two-sided Student's t-test. $P<0.05$ was considered to indicate a statistically significant difference. SPSS version 18 (SPSS, Inc., Chicago, IL, USA) was used for data management and analysis, and GraphPad Prism 7.0 (GraphPad Software, Inc., La Jolla, CA, USA) was used for Figure generation.

Results

Buparlisib significantly reduces tumour burden in vivo. A total of 1 week after tumour cell inoculation in mice, tumour growth in bones was confirmed by optical imaging (Fig. 1B-1) with an average tumour size of 0.04 cm^3 (0.01-0.09 cm^3) at week 0 for both groups. The tumour size continued to grow as expected in the control group and peaked at 3 weeks with an average size of 0.63 cm^3 (0.56-0.78 cm^3); however, in the buparlisib group, the rate of tumour growth was significantly inhibited at 1 week compared with the control group. Average tumour volume in the buparlisib group at 3 weeks was 0.10 cm^3 (0.03-0.20 cm^3), which was significantly lower than in the control group ($P=0.002$, Fig. 1B-2). Since the implanted NCI-H460 cell line expresses a firefly luciferase reporter, tumour growth in the right tibia was detected and monitored by reporter gene BLI. As shown in Fig. 1B-1, buparlisib treatment reduced bioluminescence signals in the tumour lesions,

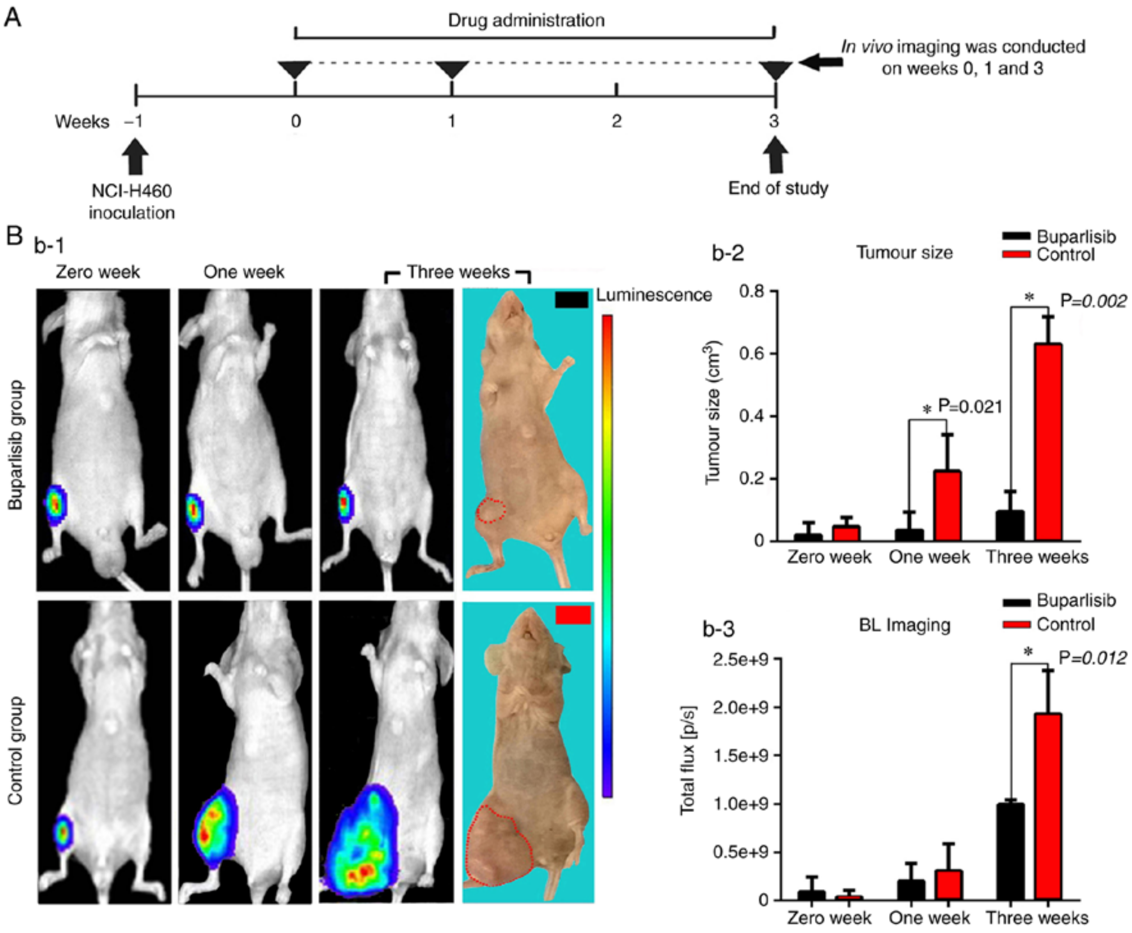

Figure 1. Treatment protocol, optical images and quantitative analysis of bone tumour-bearing mice. (A) Treatment protocol. Schematic representation of buparlisib treatment and *in vivo* imaging of the tumour model. (B-1) BLI of both groups of bone tumour-bearing mice at different time points, and photographs captured at the end of the experiment. The strength of the bioluminescence signal is correlated with tumour burden, with a pseudo-colour scale ranging from red (most intense) to violet (least intense). (B-2) Tumour volume of bone tumour-bearing mice at different time points. Buparlisib treatment markedly decreased tumour size at 1 and 3 weeks. (B-3) Bioluminescence signal of both groups of bone tumour-bearing mice at different time points. Tumour growth and activity were reduced in the buparlisib group at 3 weeks. Results are presented as the means ± standard deviation. *P<0.05. BLI, bioluminescence imaging.

indicating reduced tumour growth and activity, compared with in the control group at 3 weeks ($9.94\times10^8\pm4.70\times10^7$ photon/sec in the buparlisib group vs. $1.93\times10^9\pm4.50\times10^8$ photon/sec in the control group; P=0.012, Fig. 1B-3). These results indicated that the PI3K inhibitor buparlisib may exert antitumour activity on NCI-H460 cell growth in murine bone.

Buparlisib induces NCI-H460 cell apoptosis and reduces tumour activity in vivo. To assess the tumour metabolic activity in the right tibiae of mice in the buparlisib and control groups, the ^{18}F-FDG MicroPET/CT *in vivo* molecular imaging technique was conducted. The ^{18}F-FDG PET/CT images exhibited reduced ^{18}F-FDG metabolic activities in the tumours of the buparlisib group compared with those of the control group at 1 and 3 weeks (Fig. 2A-1). Quantitative data in the ROI were analysed in terms of SUVmax and the R/L SUVmax ratio. As presented in Fig. 2A-2, reduced uptake of ^{18}F-FDG was detected in the metaphysis region of the right tibiae in the buparlisib group compared with in the control group at 1 week (2.34±0.91 in the buparlisib group vs. 4.57±0.87 in the control group; P=0.008) and at 3 weeks (2.43±0.58 in the buparlisib group vs. 6.97±1.36 in the control group; P=0.008), respectively. In order to determine whether buparlisib-induced tumour regression in the right tibiae was attributed to induction of cell death and apoptosis, cell death was examined in a single cell suspension prepared from excised tumour tissues from both groups after 3 weeks by flow cytometry using Annexin V FITC staining. As shown in Fig. 2B1 and B2, significant apoptotic cell induction was detected in the buparlisib group compared with in the untreated control group (40.76±1.26% in the buparlisib group vs. 26.54±1.90% in the control group; P=0.008). Induction of apoptotic cell death was also confirmed by the upregulation of active caspase 3 in the buparlisib group compared with in the control group (Fig. 2C), as determined by western blot analysis. Notably, there were no alterations in the expression levels of other pro-apoptotic or anti-apoptotic proteins, including Bcl-2 and Bax. As shown in Fig. 2D, the TUNEL assay revealed that the number of TUNEL-positive cells was markedly increased in cells from mice treated with buparlisib (76.8±16.4% in the buparlisib group vs. 17.5±12.9% in the control group; P=0.0079), confirming the apoptotic effect of buparlisib on tumour cells.

Buparlisib inhibits osteoclast formation and reduces osteolytic destruction. Since buparlisib treatment resulted in tumour growth retardation and apoptotic induction in implanted

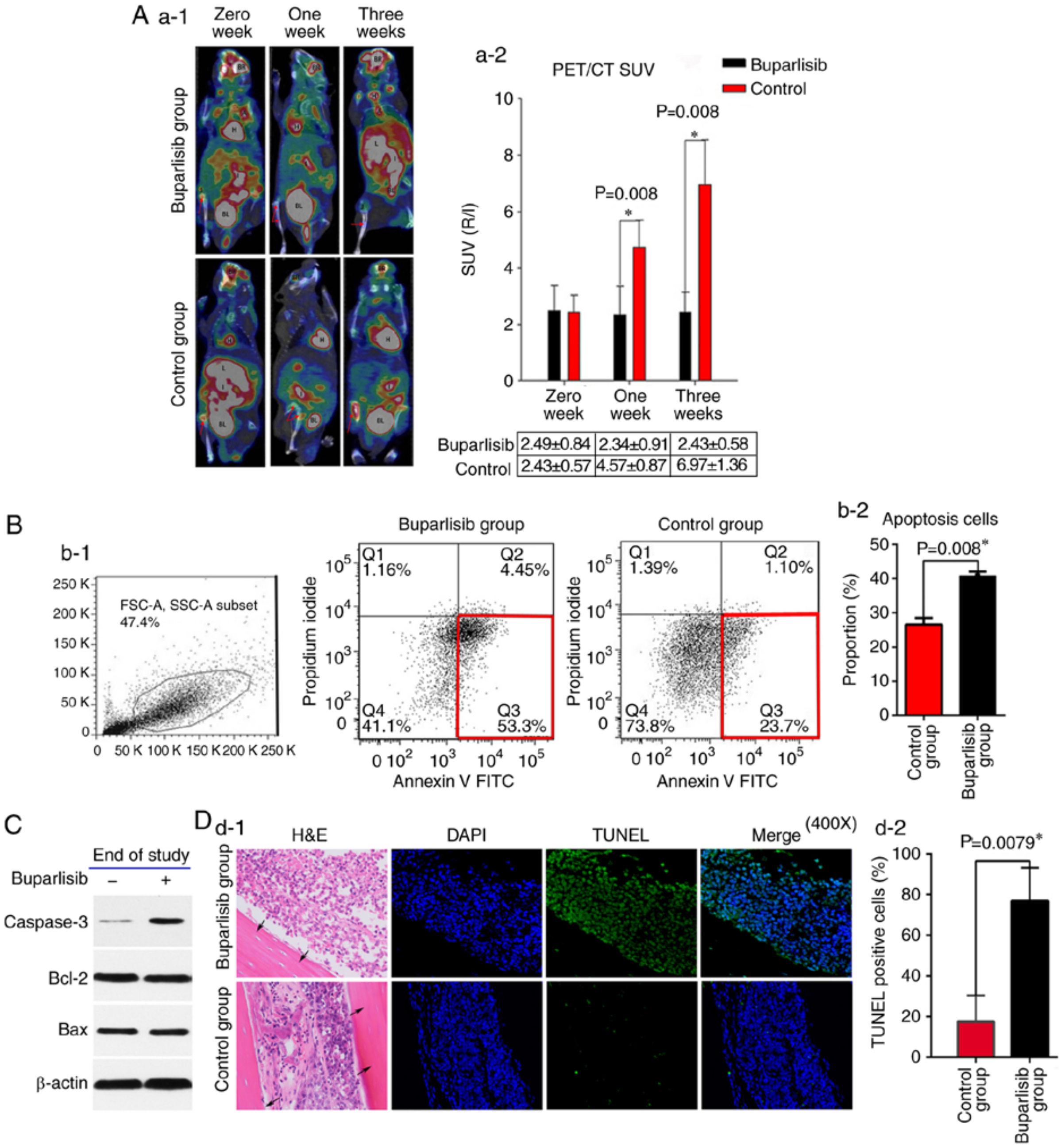

Figure 2. Buparlisib induces NCI-H460 cell apoptosis and reduces tumour activity *in vivo*. (A-1) ^{18}F-FDG PET/CT of bone tumour-bearing mice was assessed at different time points in buparlisib-treated and control mice; red arrows represent the boundaries of the ROI. Tumour burden was reduced in the ROI of the buparlisib group compared with the control group at 1 and 3 weeks. High ^{18}F-FDG uptake is considered normal in organs including the H, BR, BL and I. (A-2) Quantitative R/L ratio of SUV of bone tumour-bearing mice was assessed at the indicated time points. (B-1) Apoptotic cell death was assessed in single cell suspensions from excised tumour lesions of bone tumour-bearing mice at the end of study. NCI-H460-luc2 tumour cells were randomly isolated from three mice obtained from each group at 3 weeks after treatment, and were stained with Annexin V and analysed by fluorescence-activated cell sorting. The red frame in the right lower corner in each group indicated early apoptosis. (B-2) Quantification of data from the apoptosis assay. (C) Western blotting of tumour lesions obtained from both groups of bone tumour-bearing mice at the end of study. Caspase 3 expression, but not Bcl-2 and Bax expression, was increased in the buparlisib group at 3 weeks. β-actin was used as a loading control to ensure equal loading between samples. (D-1) Tibia sections of intraosseous NCI-H460 tumours obtained from buparlisib and control group mice at 3 weeks were stained with TUNEL and DAPI. Blue fluorescence indicated nuclei stained with DAPI. Green fluorescence indicated TUNEL-positive NCI-H460 cells in the bone marrow cavity. Black arrows indicated the cortical wall of tibiae. Magnification, x400. (D-2) Quantification of TUNEL-positive NCI-H460 cells from both groups of bone tumour-bearing mice at the end of study. The percentage of TUNEL-positive cells was higher in the buparlisib group compared with in the control group at 3 weeks. Data are presented as the means ± standard deviation. $^{*}P<0.05$. ^{18}F-FDG, 18F-fluorodeoxyglucose; A, artery; Bax, Bcl-2-associated X protein; Bcl-2, B-cell lymphoma 2; BR, brain; BL, bladder; FITC, fluorescein isothiocyanate; H, heart; H&E, haematoxylin and eosin; I, intestines; J, joint; L, liver; PET/CT, positron emission tomography/computed tomography; R/L, right/left; ROI, region of interest; SUV, standardized uptake value; TUNEL, terminal deoxynucleotidyl transferase-mediated deoxyuridine triphosphate nick end labelling.

NCI-H460 tumours, this study aimed to examine osteoclast formation and osteolytic destruction in the right tibiae of mice using the *in vivo* molecular imaging technique, ^{99m}Tc-MDP MicroSPECT/CT. As shown in Fig. 3A, markedly reduced ^{99m}Tc-MDP uptake was detected in the metaphysis region of the right tibiae at 1 and 3 weeks in the buparlisib group; however,

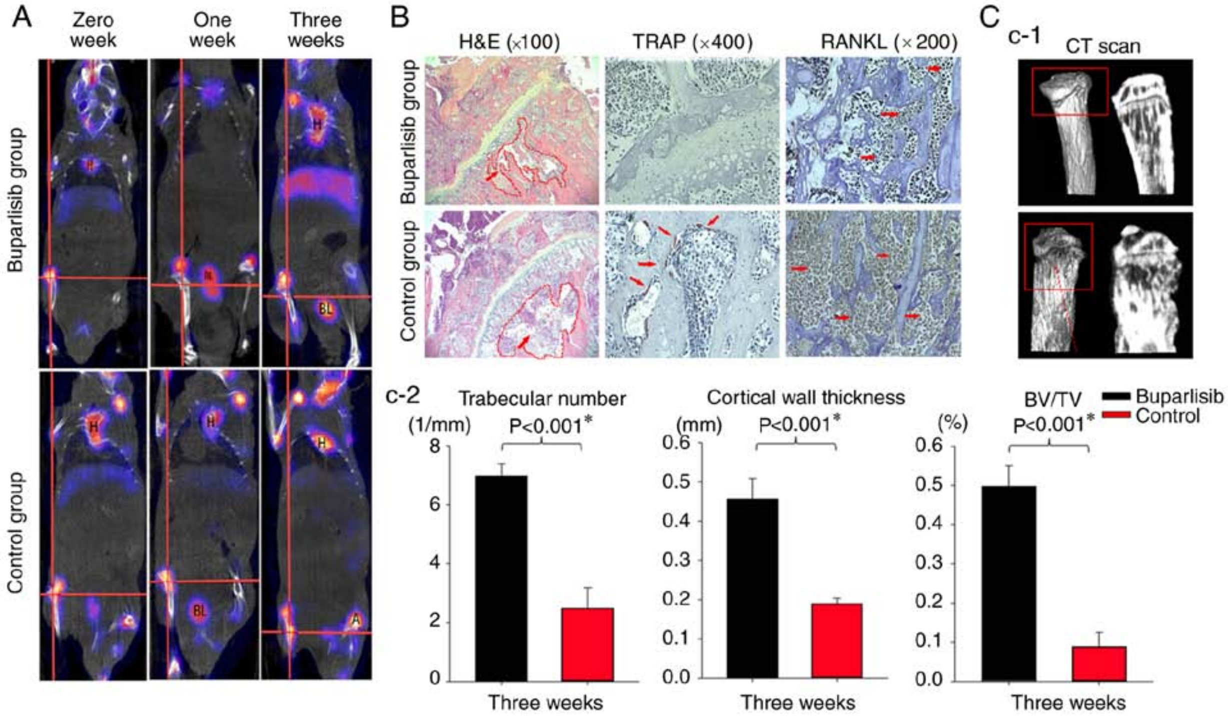

Figure 3. ^{99m}Tc-MDP SPECT/CT imaging of bone tumour-bearing mice during the whole study, and H&E staining, IHC and *ex vivo* MicroCT of tumour lesions at the end of the study. All regions shown on the histological slices were in the metaphysis. (A) ^{99m}Tc-MDP SPECT/CT imaging of both groups of bone tumour-bearing mice at different time points. SPECT/CT imaging of the mice highlighted increased radioactive uptake in the control group compared with the buparlisib group, particularly at 3 weeks, as indicated at boundaries of a region of interest, which was marked with a red cross in the centre. Organs including the H, brain, BL, liver and intestines exhibited a high uptake of ^{99m}Tc-MDP, which is considered normal. (B) H&E and IHC staining of tumour lesions at the end of the study. H&E staining revealed that more tumour cells were detected in the control group and the adjacent bone marrow cavity exhibited a loss of trabecular bone (x100 magnification; red arrows indicate tumour cells and the red dotted circle indicates the location of the marrow cavity). The protein expression levels of TRAP and RANKL were examined by IHC (red arrows indicate positive staining). The osteoclast marker TRAP was expressed in the activated osteoclast cells at the tumour bone interface, as indicated by dark purple staining. The other osteoclast marker, RANKL, exhibited dark brown staining. The levels of osteoclast markers were decreased in the buparlisib group. (C-1) *Ex vivo* MicroCT of tumour lesions at the end of study. MicroCT analysis of the proximal tibia of tumour-bearing mice revealed a marked reduction in the number of osteolytic bone lesions in the buparlisib group. Red dotted arrow in the red border indicates osteolytic bone lesions in the control group. (C-2) Quantitative analysis of ex vivo MicroCT of tumour lesions at the end of the study. Trabecular number, cortical wall thickness and BV/TV were measured in the proximal tibia of tumour-bearing mice. The number of osteolytic bone lesions was decreased in buparlisib-treated mice compared with in control mice. Data are presented as the means ± standard deviation. *P<0.05. ^{99m}Tc-MDP, ^{99m}Tc-methylene diphosphonate; A, artery; BL, bladder; BV/TV, bone volume/total volume; CT, computed tomography; H, heart; H&E, haematoxylin and eosin; IHC, immunohistochemistry; RANKL, receptor activator of nuclear factor-κB ligand; SPECT, single-photon emission computed tomography; TRAP, tartrate-resistant acid phosphatase.

this reduction was not detected in the control group. To assess histological alterations within the tibiae, sections of intraosseous NCI-H460 tumour from buparlisib-treated and untreated mice were stained with H&E after 3 weeks. As shown in the metaphysis of the upper tibia, results obtained from H&E staining suggested that fewer tumour cells were present in the bone marrow cavity, and bone destruction was reduced in the buparlisib group compared with in the control group after 3 weeks of treatment (Fig. 3B). The osteoclast markers, TRAP and RANKL, were also examined by immunohistochemistry (IHC); the results indicated that the expression of both osteoclast markers was decreased in the buparlisib group compared with in the untreated control group (Fig. 3B). Furthermore, *ex vivo* MicroCT analysis of the proximal tibia of tumour-bearing mice revealed a marked reduction in the number of osteolytic bone lesions in the buparlisib group after 3 weeks (Fig. 3C-1), alongside significantly higher quantitative bone parameters, including trabecular number (6.98±0.42 in the buparlisib group vs. 2.47±0.70 in the control group; P=3.74x10^{-5}), cortical wall thickness (0.46±0.05 in the buparlisib group vs. 0.19±0.01 in the control group; P=2.12x10^{-5}), and trabecular volume (0.50±0.05 in the buparlisib group V.S. 0.09±0.04 in the control group; P=1.62x10^{-5}) (Fig. 3C-2), thus suggesting that the PI3K inhibitor exerted anti-osteoclastogenic effects *in vivo*.

Buparlisib enhances DWB capacity and maintains body weight. To assess how quality of life is affected by the PI3K inhibitor buparlisib, body weight and DWB ability were measured at 0, 1 and 3 weeks in both groups. Notably, a slight increase in body weight was detected 1 week after buparlisib treatment compared with in the control group (23.36±3.31 g in the buparlisib group vs. 21.95±2.70 g in the control group; P=0.283; Fig. 4A); however, body weight between the two groups was comparable after 3 weeks (20.06±1.92 g in the buparlisib group vs. 21.10±1.21 g in the control group; P=0.460; Fig. 4A). Therefore, DWB tests were further performed to examine whether the control of symptoms associated with bone metastasis differed between the two groups; for DWB tests, the amount of weight passing through each paw was assessed automatically via pressure transducers. DWB ability was enhanced in the buparlisib group after 1 week compared

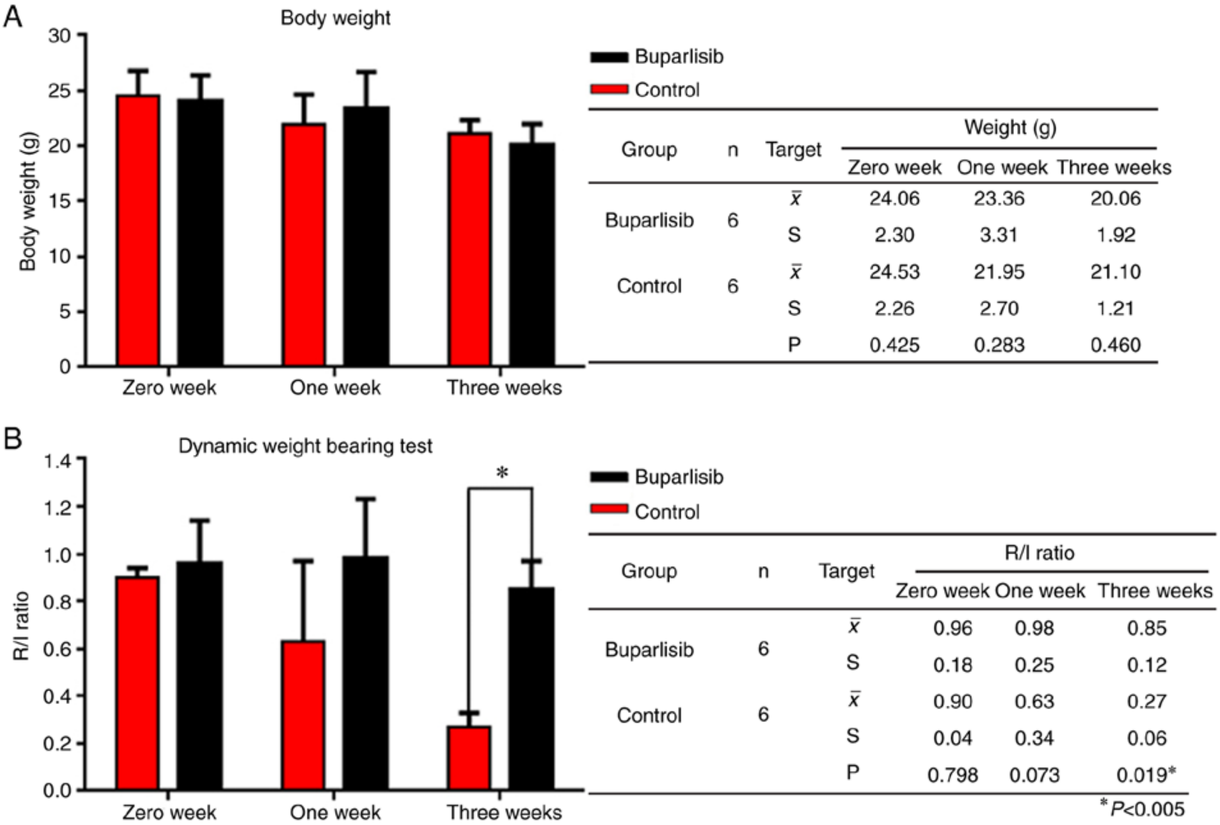

Group	n	Target	Weight (g)		
			Zero week	One week	Three weeks
Buparlisib	6	$\bar{x}$	24.06	23.36	20.06
		S	2.30	3.31	1.92
Control	6	$\bar{x}$	24.53	21.95	21.10
		S	2.26	2.70	1.21
		P	0.425	0.283	0.460

Group	n	Target	R/I ratio		
			Zero week	One week	Three weeks
Buparlisib	6	$\bar{x}$	0.96	0.98	0.85
		S	0.18	0.25	0.12
Control	6	$\bar{x}$	0.90	0.63	0.27
		S	0.04	0.34	0.06
		P	0.798	0.073	0.019*

*$P<0.005$

Figure 4. Body weight and DWB capacity of bone tumour-bearing mice during the whole study. (A) Body weight of bone tumour-bearing mice at different time points. Body weight was measured by week following the first buparlisib injection. Buparlisib treatment induced a slight increase in body weight 1 week after treatment, whereas a comparative body weight was detected between the two groups after 3 weeks. (B) DWB capacity of bone tumour-bearing mice at different time points. The average values of R/L raw pressure were calculated and analysed. DWB ability was enhanced in the buparlisib group after 1 week compared with the control group, and was significantly improved after 3 weeks. Data are presented as the means ± standard deviation. $^*P<0.05$. DWB, dynamic weight bearing; R/L, right/left.

with the control group (0.98±0.25 in the buparlisib group vs. 0.63±0.34 in the control group; P=0.073; Fig. 4B), and was significantly improved after 3 weeks (0.85±0.12 in the buparlisib group vs. 0.27±0.06 in the control group; P=0.019; Fig. 4B). These results indicated that treatment with a PI3K inhibitor could significantly increase the weight-bearing capacity of tumour-bearing limbs.

Discussion

Studies of buparlisib in patients with advanced or recurrent endometrial carcinoma and human epidermal growth factor receptor 2-positive advanced breast cancer have failed to improve the progression-free survival of patients (27,28). However, there is still scope for the use of buparlisib. Notably, PI3K pathway mutations in circulating tumour DNA are more commonly detected in metastatic tissues compared with in primary biopsies from patients with lung cancer (29). Buparlisib has good blood-brain-barrier penetrance, and PI3K inhibition may hold considerable promise in the treatment of brain metastasis and the respective microenvironment (30). Furthermore, the results from the BELLE-2 study demonstrated that buparlisib has the greatest clinical benefit and tolerable safety profile for patients with hormone receptor-positive, epidermal growth factor receptor 2-negative advanced breast cancer (31). The results of the present study indicated that targeting the PI3K pathway may prevent structural skeletal damage associated with bone metastasis of lung cancer.

Bone metastasis represents a difficult-to-treat clinical scenario, due to pain, increased skeletal-related events (SREs), decreased quality of life and diminished overall survival outcomes (32). Approved therapeutic agents in the 2017 National Comprehensive Cancer Network cancer treatment guidelines (33) for treating bone metastasis focus on treatment of significant pain and SREs. These drugs include bisphosphonates, which inhibit bone resorption through apoptotic effects on osteoclasts (34); denosumab, which is a RANKL inhibitor that prevents the development of osteoclasts that break down bone (35); radioisotopes, which are used to treat patients with osteoblastic or mixed metastatic bony lesions; hormonal therapy and chemotherapy. Although bisphosphonates are widely used in clinical practice, identification of novel compounds with combined antitumour and bone-protective effects would be highly advantageous (36).

The present study used various techniques to monitor tumour growth over the treatment course. The results demonstrated that buparlisib exerted inhibitory effects on tumour growth during the treatment course *in vivo*. The PI3K/mTOR/AKT pathway promotes osteoclastogenesis *in vitro*, suggesting that PI3K and mTOR inhibitors may be useful in the treatment of cancer-associated bone loss (37). Therefore, this study aimed to examine the effects of buparlisib on implanted

NCI-H460 (PIK3CA-mutant) tumours in the right tibiae of mice following confirmation of tumour growth. After administration of buparlisib at weeks 0, 1 and 3, bone destruction was reduced compared with in the control group, as evidenced by TRAP and RANKL staining by IHC. In addition, animals in the buparlisib-treated group maintained their DWB capability. Utilizing small animal MicroPET/CT (^{18}F-FDG) and SPECT/CT (^{99m}Tc-MDP) imaging techniques, ^{18}F-FDG and ^{99m}Tc-MDP uptake was reduced in the metaphysis region of right tibiae at 1 and 3 weeks in the buparlisib group.

Osteoclast activation is regulated by complex signalling pathways, including systemic factors and locally secreted cytokines. RANKL is naturally expressed on the membrane surface of stromal cells and osteoblasts, in addition to active T cells (38). Activation of RANK by RANKL results in osteoclast activation through signalling cascades that involve activation of the NF-κB and c-Jun N-terminal kinase pathways. The PI3K pathway regulates RANKL-induced osteoclast migration and invasion (39); sustained PI3K signalling in MM impacts osteoclastogenic potential, and enhances inflammation and local bone destruction (40). The PI3K/Akt pathway stimulates the expression of RANKL, parathyroid hormone-related protein and bone morphogenetic protein-2, partly through NF-κB, highlighting the potential therapeutic effect of the PI3K/Akt pathway in bone metastasis of prostate cancer (41). TRAP is associated with osteoclast migration to bone resorption sites, and is believed to initiate osteoclast differentiation, activation and proliferation. Therefore, osteoclasts can be identified by TRAP staining (42). In agreement with the aforementioned effects of the PI3K pathway, in the present study, buparlisib treatment reduced levels of the osteoclast markers, TRAP and RANKL, compared with the control group.

In the present study, tumour growth and burden were longitudinally assessed *in vivo* via multimodality molecular imaging techniques, including reporter gene BLI, small animal PET/CT (^{18}F-FDG) and SPECT/CT (^{99m}Tc-MDP). Multimodality molecular imaging can be defined as the visualization, characterization and quantification of biological processes at the cellular and molecular levels in living organisms; *in vivo*, this can be used to continuously monitor the metabolic and physiological progress of bone metastasis. Therefore, the mechanisms underlying disease can be studied in a physiologically intact environment (43,44). PET/CT (^{18}F-FDG) and SPECT/CT (^{99m}Tc-MDP) imaging techniques are widely used in clinical and basic research settings. In addition, luciferases are among the most sensitive probes and are considered powerful tools for visualizing live tissues and whole animals, for example through BLI. Luciferases catalyse light emission via the oxidation of small molecule substrates, known as luciferins. Since no external light is required, the background emission is virtually zero, enabling sensitive imaging *in vivo* (45). Notably, all of these imaging techniques are non-invasive.

Combining PET/CT and SPECT techniques may help to overcome the difficulties associated with quantitative analysis of metastatic lesions obtained from optical imaging (46), thereby improving understanding of bone destruction, and tracking the molecular and functional alterations of bone metastases of lung cancer using multiparametric quantification (47,48). In this study, reduced ^{18}F-FDG and ^{99m}Tc-MDP uptake was detected in the metaphysis region of the buparlisib group by PET/CT and SPECT/CT imaging, thus highlighting the antitumour activity of buparlisib and its ability to inhibit osteoclast-associated bone destruction. Taken together, these data indicated that buparlisib may possess antitumour activity, reduce bone destruction and exert protective effects against progressive bone destruction, which may guide the development of clinical trials using a combination of buparlisib and antitumour drugs.

The present study had its limitation. At present, several techniques, including direct injection into the left ventricle and orthotopic implantation are currently used to induce bone metastasis of lung cancer. Although it cannot be used to monitor the whole process of metastasis from lung to skeleton, local injection remains one of the most commonly used techniques to induce bone metastasis, due to ease of operation and consistency of growth states between animal models (49). In the present study, the bone metastatic model was established via direct implantation of NCI-H460-luc2 lung cancer cells into the right tibiae of mice. NCI-H460-luc2 cells appeared to exhibit higher tumour formation rate and adequate reproducibility compared with other NSCLC cell lines, including A549 and PC-9 (data not shown), allowing direct comparison with the normal control group. Therefore, this model may be used to determine therapeutic effects against metastatic lesions. Furthermore, the present study primarily focused on the pre-clinical activity of buparlisib on bone metastases caused by lung cancer cells; therefore, the present findings could act as a basis for clinical trials of buparlisib as a novel therapy for the treatment of patients with lung cancer and bone metastases.

In conclusion, this study indicated that the PI3K inhibitor buparlisib exerted significant inhibitory effects on the progression of osteolytic invasion by suppressing osteoclast formation and RANKL expression, as determined by analysing murine xenograft models using multimodality molecular imaging. Furthermore, the antitumour properties and favourable safety profile of this drug make it particularly attractive as a potential treatment for patients with lung cancer and bone metastases.

Acknowledgements

Not applicable.

Funding

This study was supported by the National Natural Science Foundation of China (grant nos. 81302005, 11275050 and 30700188), the Shanghai Municipality Science and Technology Commission Foundation Key Project (grant nos. 15411951602, 14JC1401400, 16401970704 and 13ZR1438500), the Ministry of Education Returned Scientific Research Foundation, Trans-Century Training Programme Foundation for the Talents by the State Education Commission (to JZ), the Youth Foundation of Shanghai Municipal Public Health Bureau (grant no. 20124Y114), the Project of Shanghai Municipal Public Health Bureau (grant no. 201840122), the Scientific Research Project of Shanghai Municipal Cadre Health Bureau [2017(12)], the Interdisciplinary Program of Shanghai Jiao Tong

University (grant no. YG2017MS80), the 'Shanghai Young Physician Development Program' of Shanghai Municipal Public Health Bureau, the second batch (2012(105)) (to XMN), and the Shanghai Engineering Research Center of Molecular Imaging Probes (grant no. 14DZ2251400).

Availability of data and materials

The datasets used and/or analysed during the current study are available from the corresponding author on reasonable request.

Authors' contributions

JieZ, MW, YW, SL and LX conceived and designed the experiments. SW, QW, XB and JianpingZ performed the experiments. SW and XN wrote the paper. SW and XN collected and analysed the data. XB and JianpingZ provided technical expertise. JieZ, MW, YW and SL provided assistance with revising this manuscript. All authors read and approved the manuscript.

Ethics approval and consent to participate

The present study was approved by the Ethics Committee of Fudan University Institutional Animal Care and Longhua Hospital, Shanghai University of Traditional Chinese Medicine. The use of animals and the experimental protocol were approved by the Institutional Animal Care and Use Committee of Longhua Hospital, Shanghai University of Traditional Chinese Medicine. All experiments were performed in accordance with relevant guidelines and regulations for the welfare and use of animals in cancer research.

Patient consent for publication

Not applicable.

Competing interests

The authors declare that they have no competing interests.

References

1. Siegel RL, Miller KD and Jemal A: Cancer statistics, 2017. CA Cancer J Clin 67: 7-30, 2017.
2. Chen W, Zheng R, Baade PD, Zhang S, Zeng H, Bray F, Jemal A, Yu XQ and He J: Cancer statistics in China, 2015. CA Cancer J Clin 66: 115-132, 2016.
3. Ferlay J, Soerjomataram I, Dikshit R, Eser S, Mathers C, Rebelo M, Parkin DM, Forman D and Bray F: Cancer incidence and mortality worldwide: Sources, methods and major patterns in GLOBOCAN 2012. Int J Cancer 136: E359-E386, 2015.
4. Riihimäki M, Hemminki A, Fallah M, Thomsen H, Sundquist K, Sundquist J and Hemminki K: Metastatic sites and survival in lung cancer. Lung Cancer 86: 78-84, 2014.
5. Coleman RE: Clinical features of metastatic bone disease and risk of skeletal morbidity. Clin Cancer Res 12 (Suppl): S6243-S6249, 2006.
6. Cheung FH: The practicing orthopedic surgeon's guide to managing long bone metastases. Orthop Clin North Am 45: 109-119, 2014.
7. Ratasvuori M, Wedin R, Hansen BH, Keller J, Trovik C, Zaikova O, Bergh P, Kalen A and Laitinen M: Prognostic role of en-bloc resection and late onset of bone metastasis in patients with bone-seeking carcinomas of the kidney, breast, lung, and prostate: SSG study on 672 operated skeletal metastases. J Surg Oncol 110: 360-365, 2014.
8. Weber KL, Randall RL, Grossman S and Parvizi J: Management of lower-extremity bone metastasis. J Bone Joint Surg Am 88 (Suppl 4): S11-S19, 2006.
9. Zhu M, Liang R, Pan LH, Huang B, Qian W, Zhong JH, Zheng WW and Li CL: Zoledronate for metastatic bone disease and pain: A meta-analysis of randomized clinical trials. Pain Med 14: 257-264, 2013.
10. Lopez-Olivo MA, Shah NA, Pratt G, Risser JM, Symanski E and Suarez-Almazor ME: Bisphosphonates in the treatment of patients with lung cancer and metastatic bone disease: A systematic review and meta-analysis. Support Care Cancer 20: 2985-2998, 2013.
11. Wong MH, Stockler MR and Pavlakis N: Bisphosphonates and other bone agents for breast cancer. Cochrane Database Syst Rev: CD003474, 2012.
12. Mhaskar R, Redzepovic J, Wheatley K, Clark OA, Miladinovic B, Glasmacher A, Kumar A and Djulbegovic B: Bisphosphonates in multiple myeloma: A network meta-analysis. Cochrane Database Syst Rev: CD003188, 2012.
13. Peng X, Guo W, Ren T, Lou Z, Lu X, Zhang S, Lu Q and Sun Y: Differential expression of the RANKL/RANK/OPG system is associated with bone metastasis in human non-small cell lung cancer. PLoS One 8: e58361, 2013.
14. Mundy GR: Metastasis to bone: Causes, consequences and therapeutic opportunities. Nat Rev Cancer 2: 584-593, 2002.
15. Cappuzzo F, Ligorio C, Jänne PA, Toschi L, Rossi E, Trisolini R, Paioli D, Holmes AJ, Magrini E, Finocchiaro G, *et al*: Prospective study of gefitinib in epidermal growth factor receptor fluorescence in situ hybridization-positive/phospho-Akt-positive or never smoker patients with advanced non-small-cell lung cancer: The ONCOBELL trial. J Clin Oncol 25: 2248-2255, 2007.
16. Tsurutani J, Fukuoka J, Tsurutani H, Shih JH, Hewitt SM, Travis WD, Jen J and Dennis PA: Evaluation of two phosphorylation sites improves the prognostic significance of Akt activation in non-small-cell lung cancer tumors. J Clin Oncol 24: 306-314, 2006.
17. Chan BA and Hughes BG: Targeted therapy for non-small cell lung cancer: Current standards and the promise of the future. Transl Lung Cancer Res 4: 36-54, 2015.
18. La Monica S, Galetti M, Alfieri RR, Cavazzoni A, Ardizzoni A, Tiseo M, Capelletti M, Goldoni M, Tagliaferri S, Mutti A, *et al*: Everolimus restores gefitinib sensitivity in resistant non-small cell lung cancer cell lines. Biochem Pharmacol 78: 460-468, 2009.
19. Sos ML, Fischer S, Ullrich R, Peifer M, Heuckmann JM, Koker M, Heynck S, Stückrath I, Weiss J, Fischer F, *et al*: Identifying genotype-dependent efficacy of single and combined PI3K- and MAPK-pathway inhibition in cancer. Proc Natl Acad Sci USA 106: 18351-18356, 2009.
20. Zito CR, Jilaveanu LB, Anagnostou V, Rimm D, Bepler G, Maira SM, Hackl W, Camp R, Kluger HM and Chao HH: Multi-level targeting of the phosphatidylinositol-3-kinase pathway in non-small cell lung cancer cells. PLoS One 7: e31331, 2012.
21. Engelman JA, Chen L, Tan X, Crosby K, Guimaraes AR, Upadhyay R, Maira M, McNamara K, Perera SA, Song Y, *et al*: Effective use of PI3K and MEK inhibitors to treat mutant Kras G12D and PIK3CA H1047R murine lung cancers. Nat Med 14: 1351-1356, 2008.
22. Maira SM, Pecchi S, Huang A, Burger M, Knapp M, Sterker D, Schnell C, Guthy D, Nagel T, Wiesmann M, *et al*: Identification and characterization of NVP-BKM120, an orally available pan-class I PI3-kinase inhibitor. Mol Cancer The 11: 317-328, 2013.
23. Speranza MC, Nowicki MO, Behera P, Cho CF, Chiocca EA and Lawler SE: BKM-120 (Buparlisib): A Phosphatidyl-Inositol-3 kinase inhibitor with anti-invasive properties in glioblastoma. Sci Rep 6: 20189, 2016.
24. Ren H, Chen M, Yue P, Tao H, Owonikoko TK, Ramalingam SS, Khuri FR and Sun SY: The combination of RAD001 and NVP-BKM120 synergistically inhibits the growth of lung cancer in vitro and in vivo. Cancer Lett 325: 139-146, 2012.
25. Wu TT, Sikes RA, Cui Q, Thalmann GN, Kao C, Murphy CF, Yang H, Zhau HE, Balian G and Chung LW: Establishing human prostate cancer cell xenografts in bone: Induction of osteoblastic reaction by prostate-specific antigen-producing tumors in athymic and SCID/bg mice using LNCaP and lineage-derived metastatic sublines. Int J Cancer 77: 887-894, 1998.
26. Quadros AU, Pinto LG, Fonseca MM, Kusuda R, Cunha FQ and Cunha TM: Dynamic weight bearing is an efficient and predictable method for evaluation of arthritic nociception and its pathophysiological mechanisms in mice. Sci Rep 5: 14648, 2015.

27. Heudel PE, Fabbro M, Roemer-Becuwe C, Kaminsky MC, Arnaud A, Joly F, Roche-Forestier S, Meunier J, Foa C, You B, *et al*: Phase II study of the PI3K inhibitor BKM120 in patients with advanced or recurrent endometrial carcinoma: A stratified type I-II study from the GINECO group. Br J Cancer: 116: 303-309, 2017.
28. Martín M, Chan A, Dirix L, O'Shaughnessy J, Hegg R, Manikhas A, Shtivelband M, Krivorotko P, Batista López N, Campone M, *et al*: A randomized adaptive phase II/III study of buparlisib, a pan-class I PI3K inhibitor, combined with paclitaxel for the treatment of HER2- advanced breast cancer (BELLE-4). Ann Oncol 28: 313-320, 2017.
29. Vansteenkiste JF, Canon JL, De Braud F, Grossi F, De Pas T, Gray JE, Su WC, Felip E, Yoshioka H, Gridelli C, *et al*: Safety and efficacy of Buparlisib (BKM120) in patients with PI3K pathway-activated non-small cell lung cancer: Results from the phase II BASALT-1 study. J Thorac Oncol 10: 1319-1327, 2015.
30. Blazquez R, Wlochowitz D, Wolff A, Seitz S, Wachter A, Perera-Bel J, Bleckmann A, Beißbarth T, Salinas G, Riemenschneider MJ, *et al*: PI3K: A master regulator of brain metastasis-promoting macrophages/microglia. Glia 66: 2438-2455, 2018.
31. Campone M, Im SA, Iwata H, Clemons M, Ito Y, Awada A, Chia S, Jagiełło-Gruszfeld A, Pistilli B, Tseng LM, *et al*: Buparlisib plus fulvestrant versus placebo plus fulvestrant for postmenopausal, hormone receptor-positive, human epidermal growth factor receptor 2-negative, advanced breast cancer: Overall survival results from BELLE-2. Eur J Cancer 103: 147-154, 2018.
32. Gdowski AS, Ranjan A and Vishwanatha JK: Current concepts in bone metastasis, contemporary therapeutic strategies and ongoing clinical trials. J Exp Clin Cancer Res 36: 108, 2017.
33. National Comprehensive Cancer Network Clinical Practice in Oncology (NCCN Guideline), 2017, https://www.nccn.org/professionals/physician_gls/pdf/nscl.pdf.
34. Saad F, Gleason DM, Murray R, Tchekmedyian S, Venner P, Lacombe L, Chin JL, Vinholes JJ, Goas JA and Zheng M; Zoledronic Acid Prostate Cancer Study Group: Long-term efficacy of zoledronic acid for the prevention of skeletal complications in patients with metastatic hormone-refractory prostate cancer. J Natl Cancer Inst 96: 879-882, 2014.
35. Fizazi K, Carducci M, Smith M, Damião R, Brown J, Karsh L, Milecki P, Shore N, Rader M, Wang H, Jiang Q, *et al*: Denosumab versus zoledronic acid for treatment of bone metastases in men with castration-resistant prostate cancer: A randomised, double-blind study. Lancet 377: 813-822, 2011.
36. Lipton A, Fizazi K, Stopeck AT, Henry DH, Brown JE, Yardley DA, Richardson GE, Siena S, Maroto P, Clemens M, *et al*: Superiority of denosumab to zoledronic acid for prevention of skeletal-related events: A combined analysis of 3 pivotal, randomised, phase 3 trials. Eur J Cancer 48: 3082-3092, 2012.
37. Gan ZY, Fitter S, Vandyke K, To LB, Zannettino AC and Martin SK: The effect of the dual PI3K and mTOR inhibitor BEZ235 on tumour growth and osteolytic bone disease in multiple myeloma. Eur J Haematol 94: 343-354, 2015.
38. Roodman GD: Mechanisms of bone metastasis. N Engl J Med 350: 1655-1664, 2004.
39. Xuan W, Feng X, Qian C, Peng L, Shi Y, Xu L, Wang F and Tan W: Osteoclast differentiation gene expression profiling reveals chemokine CCL4 mediates RANKL-induced osteoclast migration and invasion via PI3K pathway. Cell Biochem Funct 35: 171-177, 2017.
40. Blüml S, Friedrich M, Lohmeyer T, Sahin E, Saferding V, Brunner J, Puchner A, Mandl P, Niederreiter B, Smolen JS, *et al*: Loss of phosphatase and tensin homolog (PTEN) in myeloid cells controls inflammatory bone destruction by regulating the osteoclastogenic potential of myeloid cells. Ann Rheum Dis 74: 227-233, 2015.
41. Zhu W, Hu X, Xu J, Cheng Y, Shao Y and Peng Y: Effect of PI3K/Akt signaling pathway on the process of prostate cancer metastasis to bone. Cell Biochem Biophys 72: 171-177, 2015.
42. Ek-Rylander B, Flores M, Wendel M, Heinegård D and Andersson G: Dephosphorylation of osteopontin and bone sialoprotein by osteoclastic tartrate-resistant acid phosphatase. Modulation of osteoclast adhesion in vitro. J Biol Chem 269: 14853-14856, 1994.
43. Momcilovic M and David B: Imaging cancer metabolism. Biomol Ther (Seoul) 26: 81-92, 2018.
44. Schober O and Riemann B: Recent results in cancer research: Molecular imaging in oncology. Springer-Verlag Berlin Heidelberg, Vol. 187, 2012.
45. Yao Z, Zhang BS and Prescher JA: Advances in bioluminescence imaging: New probes from old recipes. Curr Opin Chem Biol 45: 148-156, 2018.
46. Cook G Jr, Parker C, Chua S, Johnson B, Aksnes AK and Lewington VJ: 18F-fluoride PET: Changes in uptake as a method to assess response in bone metastases from castrate-resistant prostate cancer patients treated with 223Ra-chloride (Alpharadin). EJNMMI Res 1: 4, 2011.
47. Bao X, Wang MW, Luo JM, Wang SY, Zhang YP and Zhang YJ: Optimization of early response monitoring and prediction of cancer antiangiogenesis therapy via noninvasive PET molecular imaging strategies of multifactorial bioparameters. Theranostics 6: 2084-2098, 2016.
48. Zhang F, Zhu L, Liu G, Hida N, Lu G, Eden HS, Niu G and Chen X: Multimodality imaging of tumor response to doxil. Theranostics 1: 302-309, 2011.
49. Werbeck JL, Thudi NK, Martin CK, Premanandan C, Yu L, Ostrowksi MC and Rosol TJ: Tumor microenvironment regulates metastasis and metastasis genes of mouse MMTV-PymT mammary cancer cells in vivo. Vet Pathol 51: 868-881, 2014.